Histone ADP-ribosylation promotes resistance to PARP inhibitors by facilitating PARP1 release from DNA lesions

Siham Zentout, Victor Imburchia, Catherine Chapuis, Lena Duma, Kira Schützenhofer, Evgeniia Prokhorova, Ivan Ahel, Rebecca Smith, Sébastien Huet

PNAS RESEARCH ARTICLE | CELL BIOLOGY

Histone ADP-ribosylation promotes resistance to PARP inhibitors by facilitating PARP1 release from DNA lesions

Siham Zentout[a], Victor Imburchia[a], Catherine Chapuis[a], Lena Duma[b], Kira Schützenhofer[b], Evgeniia Prokhorova[b], Ivan Ahel[b], Rebecca Smith[a,b,1], and Sébastien Huet[a,1]

Edited by Karolin Luger, University of Colorado Boulder, Boulder, CO; received December 22, 2023; accepted May 7, 2024

Poly(ADP-ribose) polymerase 1 (PARP1) has emerged as a central target for cancer therapies due to the ability of PARP inhibitors to specifically kill tumors deficient for DNA repair by homologous recombination. Upon DNA damage, PARP1 quickly binds to DNA breaks and triggers ADP-ribosylation signaling. ADP-ribosylation is important for the recruitment of various factors to sites of damage, as well as for the timely dissociation of PARP1 from DNA breaks. Indeed, PARP1 becomes trapped at DNA breaks in the presence of PARP inhibitors, a mechanism underlying the cytotoxitiy of these inhibitors. Therefore, any cellular process influencing trapping is thought to impact PARP inhibitor efficiency, potentially leading to acquired resistance in patients treated with these drugs. There are numerous ADP-ribosylation targets after DNA damage, including PARP1 itself as well as histones. While recent findings reported that the automodification of PARP1 promotes its release from the DNA lesions, the potential impact of other ADP-ribosylated proteins on this process remains unknown. Here, we demonstrate that histone ADP-ribosylation is also crucial for the timely dissipation of PARP1 from the lesions, thus contributing to cellular resistance to PARP inhibitors. Considering the crosstalk between ADP-ribosylation and other histone marks, our findings open interesting perspectives for the development of more efficient PARP inhibitor-driven cancer therapies.

DNA repair | PARP1 | ADP-ribosylation | chromatin | fluorescence microscopy

Significance

The cytotoxicity of PARP inhibitors used in the clinic to treat tumors with deficiencies in homology-directed repair mainly relies on the trapping of inhibited PARP1 on DNA breaks. Nevertheless, a complete description of the mechanisms modulating PARP1 trapping is still missing. In this study, we demonstrate that besides PARP1 automodification, the ADP-ribosylation of other targets also contributes to the timely removal of PARP1 from the breaks. In particular, we report that histone ADP-ribosylation is crucial for PARP1 mobilization, thus promoting cell resistance to PARP inhibitors.

One of the earliest detectable events of the DNA damage response (DDR) is the rapid increase in ADP-ribosylation signaling at the sites of damage (1), which is mainly triggered by the poly(ADP-ribose) polymerase 1 (PARP1). Upon binding to DNA breaks, PARP1 undergoes a conformational rearrangement to enter an active state allowing it to ADP-ribosylate nearby proteins (2). Recent findings also showed that ADP-ribosylation homeostasis relies critically on the PARP1 cofactor Histone Poly ADP-ribosylation Factor 1 (HPF1/C4ORF27) in the context of the DDR (3). HPF1 binding to PARP1 creates a composite catalytic site that is essential to control the rate of ADP-ribosylation as well as the targeting of this mark to specific amino acid residues (4–7). While multiple proteins can be ADP-ribosylated, the main acceptors in the context of the DDR are PARP1 itself and histones (3). Upon loss of HPF1, PARP1 automodification is perturbed, occurring primarily on glutamate residues instead of the preferred serine residues, and other targets, in particular histones, display massively reduced ADP-ribosylation (8, 9). While the PARP1/HPF1 complex is the main ADP-ribosylation writer within the nucleus, several actors are responsible for erasing this mark. Poly(ADP-ribose) glycohydrolase (PARG) exhibits both exo- and endo-hydrolase activities at the bonds between two ADP-ribose (ADPr) moieties but cannot hydrolyse the bond between the target residue and the first ADPr unit (10). The removal of this proximal ADPr is performed by hydrolases that are specific to a given residue, such as ARH3 for serine residues (11). The opposite activities of the writer and erasers ensure the rapid turnover of ADPr chains in the early stages of the DDR (12).

The initial activation of PARP1 and subsequent ADP-ribosylation play a central role in the DDR as the loss of PARP1 leads to a dramatic reduction in DNA repair efficiency (13). As a signaling pathway, ADP-ribosylation promotes the rapid recruitment of repair proteins bearing dedicated ADPr reading domains to sites of damage (10). It also triggers early chromatin remodeling steps facilitating access to the sites of damage for repair factors (14–16). Finally, the last crucial function of ADP-ribosylation signaling identified to date is the timely removal of PARP1 from the sites of damage. Indeed, if PARP1 is central at the early stages of the DDR, its ADP-ribosylation-dependent release from DNA breaks is also essential to proceed to the subsequent repair steps (17). Upon inhibition of its catalytic activity, PARP1 shows persistent accumulation at sites of damage, a phenomenon known as PARP trapping, which is thought to prevent access to breaks for other repair

Author affiliations: [a]University of Rennes, CNRS, Institut de génétique et développement de Rennes–UMR 6290, Biologie, Santé, Innovation Technologique (BIOSIT)–UMS3480, Rennes F-35000, France; and [b]Sir William Dunn School of Pathology, University of Oxford, Oxford OX1 3RE, United Kingdom

Author contributions: R.S. and S.H. designed research; S.Z., V.I., L.D., K.S., and R.S. performed research; C.C., E.P., and I.A. contributed new reagents/analytic tools; S.Z., V.I., L.D., K.S., and R.S. analyzed data; and S.Z., R.S., and S.H. wrote the paper.

The authors declare no competing interest.

This article is a PNAS Direct Submission.

[1]To whom correspondence may be addressed. Email: rebecca.smith@path.ox.ac.uk or sebastien.huet@univ-rennes.fr.

This article contains supporting information online at https://www.pnas.org/lookup/suppl/doi:10.1073/pnas.2322689121/-/DCSupplemental.

Published June 12, 2024.

factors (18). This trapping phenomenon has major clinical implications since it is responsible for the hypersensitivity of tumors with deficiencies in double-strand break repair by homologous recombination to PARP inhibitors (PARPi) (17). PARPi are now used in the clinic to treat BRCA-mutated tumors, and their therapeutic indications are rapidly growing (19). Yet, a better understanding of the cellular mechanisms modulating PARP1 trapping is needed to reduce the risks of acquired resistance frequently observed during these PARPi-driven therapies (20).

Inhibition of ADP-ribosylation is the central driving force of the trapping process, and any mechanism counteracting this inhibition, for example, due to the loss or mutation of the ADPr hydrolases PARG or ARH3, will promote resistance to PARPi (21, 22). Because PARP1 itself is the major target of ADP-ribosylation, it is generally thought that the electrostatic repulsion between automodified PARP1 and DNA is the main trigger of the rapid dissociation of PARP1 from the lesions (23). In line with this idea, it was reported that mutating the main residues targeted by ADP-ribosylation on PARP1 promotes trapping and renders cells more sensitive to PARPi (22). This is in addition to several other mechanisms have also been shown to impact PARP1 trapping efficiency (18, 24–28). In the present work, we describe our findings showing the specific involvement of histone ADP-ribosylation in the removal of PARP1 from the DNA lesions, thus impacting the cytotoxicity of PARPi.

Results

Increased PARP1 Trapping upon Loss of HPF1 Is Not Solely Due to Impaired Automodification. To analyze PARP1 dynamics at DNA lesions, we expressed fluorescently tagged wild-type (WT) PARP1 proteins in U2OS PARP1 knockout (KO) cells and used live-cell confocal imaging to monitor the accumulation of PARP1 to DNA lesions induced by irradiating Hoechst-sensitized nuclei with a continuous 405 nm laser (Fig. 1*A*). In agreement with previous reports, following a rapid accrual in the irradiated region, PARP1 proteins were progressively mobilized with a characteristic dissipation time of few tens of seconds (Fig. 1 *B* and *C*) (29, 30). PARP1 is ADP-ribosylated on three main residues, S499, S507, and S519, located in the automodification domain (31). The ADP-ribosylation of these three residues, which requires the association of PARP1 with its cofactor HPF1, was recently shown to contribute to the removal of PARP1 from DNA lesions (22). Confirming these findings, we observed that a PARP1 mutant with the three main ADPr acceptor residues mutated into alanine (S499A, S507A, and S519A, later referred to as 3SA), expressed in PARP1 KO cells, displayed longer retention at sites of damage induced by laser irradiation compared to its WT counterpart (Fig. 1).

Next, we wondered whether the increased trapping reported upon loss of HPF1 (22) could be fully explained by the loss of PARP1 automodification on the three main serine residues. To address this question, we compared the recruitment kinetics of PARP1-3SA in PARP1 KO and PARP1/HPF1 KO cells and found that the absence of HPF1 enhanced the trapping of this mutant (Fig. 1). Since HPF1 is not only required for the automodification of PARP1 but also for the ADP-ribosylation of several other target proteins (later referred to as heteromodification) (9), our results suggest that this latter component of ADPr signaling could also contribute to the timely removal of PARP1 from the lesions. Nevertheless, the loss of HPF1 does not simply suppress PARP1 automodification but rather leads to a switch of the ADP-ribosylation targets from the three serine residues mentioned earlier to glutamate residues and also likely modifies the characteristics of the ADPr chains that are generated along PARP1 (3, 31). This additional impact of HPF1 loss may thus partially blur the specific contribution of heteromodification on PARP1 dynamics at sites of damage.

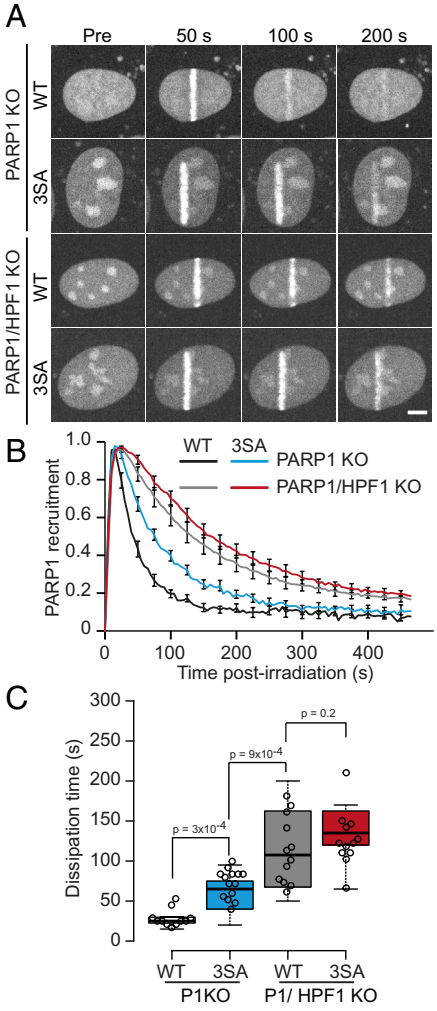

Fig. 1. Increased PARP1 trapping upon loss of HPF1 is not solely due to impaired automodification. (*A* and *B*) Representative image time courses (*A*) and recruitment kinetics (*B*) of GFP-tagged PARP1 WT and PARP1 3SA after DNA damage by 405 nm laser irradiation in PARP1 KO and PARP1/HPF1 double KO cells. (Scale bar, 5 μm.) (*C*) PARP1 release speed was assessed for each condition by estimating the characteristic dissipation time, defined as the time needed to dissipate half of the maximum recruitment intensity on the recruitment curves shown in (*B*).

Heteromodification Contributes to the Mobilisation of PARP1 from the DNA Lesions. In order to more specifically investigate the potential contribution of heteromodification on PARP1 trapping, we tested whether this component of ADP-ribosylation signaling was able to promote the release of an inactive PARP1 protein. We analyzed the recruitment dynamics of the catalytically impaired mutant PARP1 E988K (32) tagged with mCherry, expressed alone or together with GFP-tagged PARP1 WT in PARP1 KO cells. When expressed alone, PARP1 E988K did not show any dissipation from the lesions within the recorded timeframe (Fig. 2 *A* and *B*), in line with previous findings (29). In contrast, in cells coexpressing PARP1 WT, PARP1 E988K was progressively released from the lesions (Fig. 2 *A* and *B*). This release could be the consequence of heteromodification by PARP1 WT. Nevertheless, it could also be due to PARP1 automodification occurring in *trans*, which was shown to happen in vitro although less efficiently than in *cis* (33). Therefore, to be able to demonstrate a specific impact of heteromodification on PARP1 trapping, we tested whether PARP1 WT could modify PARP1 E988K in *trans* in living cells.

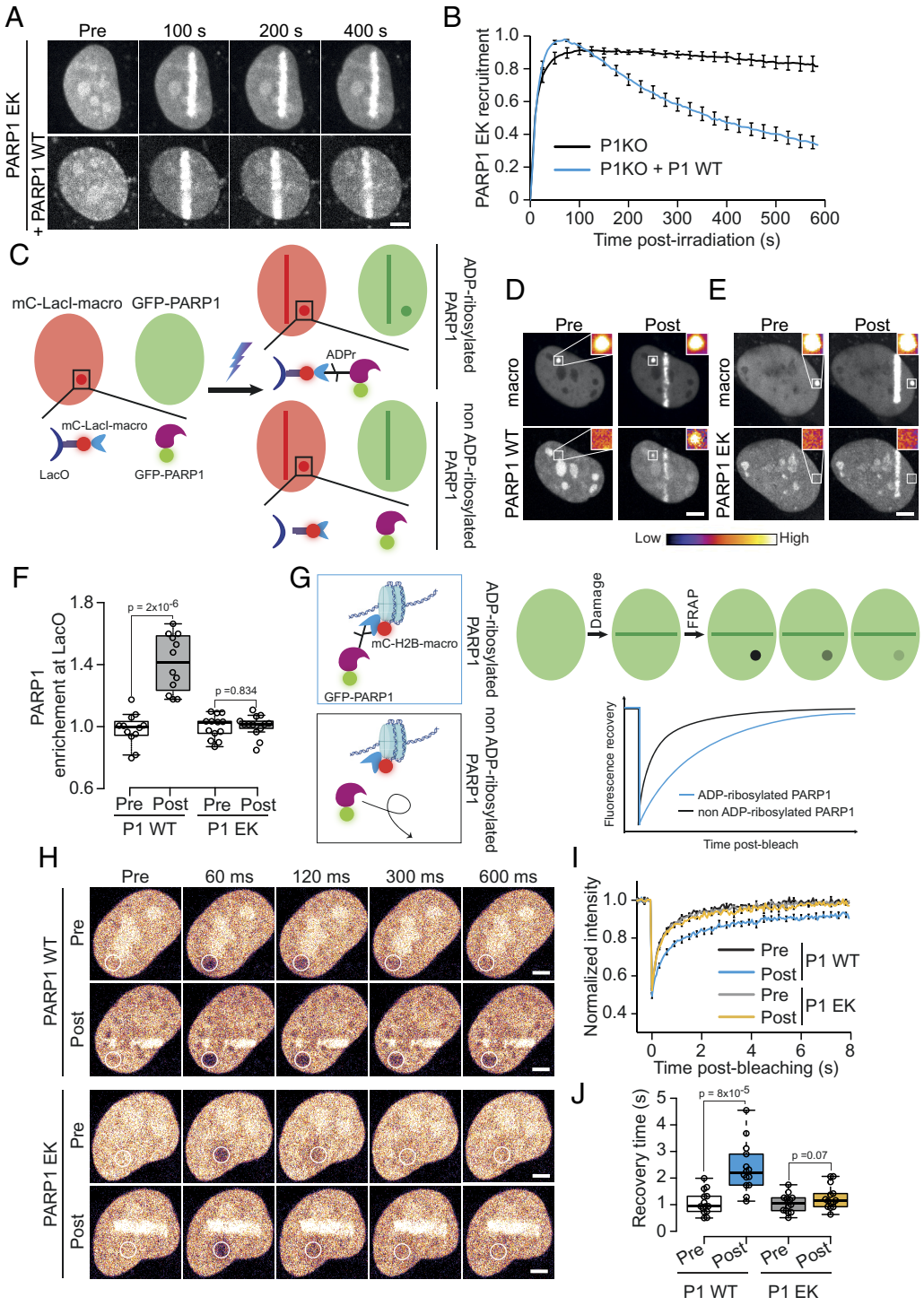

Fig. 2. Heteromodification contributes to the mobilisation of PARP1 from the DNA lesions. (*A* and *B*) Representative image time courses (*A*) and recruitment kinetics (*B*) of mCherry-tagged PARP1 E988K after DNA damage by 405 nm laser irradiation, in PARP1 KO coexpressing, or not, GFP-tagged PARP1 WT. (*C*) Schematic representation of the fluorescence two-hybrid assay used to monitor the level of PARP1 ADP-ribosylation in living cells. The mCherry-tagged fusion between the LacI and the macrodomain of macroH2A1.1 is tethered to the LacO array, thus appearing as a bright spot in the nucleus. After DNA damage by laser irradiation away from the LacO array, GFP-tagged PARP1 will enrich at the LacO array depending on its ADP-ribosylation status. (*D* and *E*) Representative images of UO2S cells bearing LacO repeats and coexpressing a mCherry-tagged fusion between the LacI and the macrodomain of macroH2A1.1 and GFP-tagged PARP1 WT (*D*) or PARP1 E988K (*E*). Images were taken prior to damage and 50 s post 405 nm laser irradiation. *Insets* pseudocolored according to the look-up table displayed below show magnification of the LacO array. (*F*) Quantification of the PARP1 accumulation at the LacO array from the images shown in (*D* and *E*). (*G*) Schematic representation of the FRAP assay used to monitor the level of PARP1 ADP-ribosylation in living cells. Cells are coexpressing a mCherry-tagged fusion between H2B and the macrodomain of macroH2A1.1 (H2B-macro) and GFP-tagged PARP1. After DNA damage by laser irradiation, the diffusion of ADP-ribosylated PARP1 within the nucleus is slowed down by its binding to the H2B-macro fusion. This slowing-down is assessed by measuring FRAP a region of interest away from the damaged region. (*H*) Representative time-course images of the FRAP of a circular area (white circle) within the nucleus of U2OS PARP1 KO cells expressing GFP-tagged PARP1 WT alone or coexpressing GFP-tagged PARP1 E988K and mCherry-tagged PARP1 WT before (pre) and 60 s after (post) 405 nm laser irradiation. Images are pseudocolored according to the look-up table shown on panel (*D*). (*I*) Normalized fluorescence recovery curves for GFP-tagged PARP1 WT and E988K obtained from the images shown in (*H*). (*J*) Characteristic recovery times estimated from the fit of the curves shown in (*I*). Scale bar, 5 μm for (*A*, *D*, *E*, and *H*).

We coexpressed a mCherry-tagged fusion of the Lac repressor (LacI) with the macrodomain of macroH2A1.1, a well-known ADPr-binding domain (34), and GFP-tagged PARP1 WT or E988K, in U2OS cells integrating a Lac operator (LacO) array (Fig. 2*C*). Upon 405 nm laser irradiation away from the LacO array, GFP-tagged PARP1 WT quickly recruited to damage, became ADP-ribosylated, and was released from the irradiated region. The consecutive increase in GFP fluorescence at the LacO array accumulating at the mCherry-tagged LacI-macrodomain fusion showed that the automodified form of PARP1 WT diffusing within the nucleus was efficiently captured by the macrodomain (Fig. 2 *D* and *F*). In contrast, when analyzing the behavior PARP1 E988K, we did not observe any accumulation at the LacO array after damage, suggesting that this mutant is not ADP-ribosylated despite the presence of endogenous PARP1 in these cells (Fig. 2 *E* and *F*). Importantly, this absence of accumulation at the LacO array was not due to a stable association of PARP1 E988K with the lesions, preventing this mutant from diffusing through the nucleoplasm to reach the LacO array. Indeed, we, and others, have previously shown that catalytically inactive PARP1 is not stably bound to the lesions and thus could efficiently diffuse through the nucleus despite displaying sustained accumulation in the irradiation area (18, 30). These data suggest that PARP1 automodification does not occur in *trans* with our current DNA damage conditions. Nevertheless, when inducing DNA breaks by irradiating non-presensitized cells with a pulsed infrared laser, we were able to detect automodification in *trans* as shown by the accumulation of ADP-ribosylated PARP1 E988K at the LacO array after DNA damage (*SI Appendix*, Fig. S1 *A* and *B*). Given that irradiation with pulsed infrared laser is thought to generate a high density of DNA breaks (35), these findings are in line with previous in vitro data suggesting that automodification can occur in *trans* when two PARP1 molecules bind onto sufficiently close-by lesions (33).

To confirm that active PARP1 was not ADP-ribosylating PARP1 E988K in *trans* with our classical 405 nm irradiation conditions, we also developed an alternative assay. We used a fusion between the macrodomain of macroH2A1.1 and H2B as a bait to immobilize ADP-ribosylated PARP1 on the chromatin within the nucleoplasm. This immobilization was assessed by fluorescence recovery after photobleaching (FRAP) of fluorescently tagged PARP1 before and after damage induction by 405 nm laser irradiation (Fig. 2*G*). While the binding of automodified PARP1 WT to the H2B-macro bait resulted in a slower FRAP recovery after damage, the mobility of PARP1 E988K remained unchanged, in line with the absence of ADPr moieties on this mutant (Fig. 2 *H*–*J*).

Given these consistent findings against automodification in *trans* upon DNA damage by 405 nm irradiation, the accelerated release of PARP1 E988K upon coexpression of PARP1 WT in PARP1 KO cells (Fig. 2 *A* and *B*) supports the idea that heteromodification contributes to PARP1 mobilization from the DNA lesions. This is further supported by the fact that the coexpression of PARP1 WT was also able to promote the mobilization of PARP1 E988K mutated at the three serine residues targeted for automodification (PARP1 3SA-E988K) (*SI Appendix*, Fig. S1*C*). Finally, given that the catalytically active, but not automodified, PARP1 3SA mutant is also able to promote the dissipation of PARP1 E988K, we can exclude that this effect is the consequence of a repulsive impact of an automodified PARP1 molecule on another nonmodified one (*SI Appendix*, Fig. S1*D*). Therefore, these different experiments provide compelling evidence in favor of the key contribution of heteromodification to PARP1 release.

Spontaneous Increase of Heteromodification Is Sufficient to Impair PARP1 Association with DNA. Besides the crucial role played by ADP-ribosylation, the exact molecular mechanisms underlying PARP1 release from DNA lesions remain unclear. Both electrostatic repulsion due to negatively charged ADPr or competition with other repair factors such as ligase 3 may promote PARP1 dissociation from the lesions (27, 36, 37). To further investigate this question and in particular assess the contribution of heteromodification, we monitored PARP1 behavior in ARH3 KO cells treated with PARG inhibitors for 48 h, which were shown to display a spontaneous increase of ADP-ribosylation signaling, in particular on histones, in contrast to ARH3-proficient cells (38). Importantly, this increase is not due to the accumulation of DNA lesions in cells lacking ARH3 since similar levels of γH2AX signaling, a key indicator of DNA breaks, were observed in WT and ARH3 KO cells treated with PARGi (38). Using fluorescence correlation spectroscopy (FCS), we found that PARP1 showed increased mobility in ARH3 KO cells, but not in WT cells, upon PARGi treatment (Fig. 3 *A* and *B* and *SI Appendix*, Fig. S2). Given that PARP1 constantly samples the DNA searching for DNA lesions (39), this increased mobility indicates impaired binding to chromatin (15). This could be the consequence of a competition between PARP1 and other repair factors for binding to DNA lesions in relation to the slight activation of the DDR associated to PARGi treatment. However, the fact that the DDR activation is observed in both WT and ARH3 KO cells while PARP1 dynamics is affected only in cells lacking ARH3 KO, goes against this possibility. Instead, these data suggest that increased ADP-ribosylation is, per se, sufficient to impair PARP1 binding to DNA independently of the presence of DNA lesions. Furthermore, since

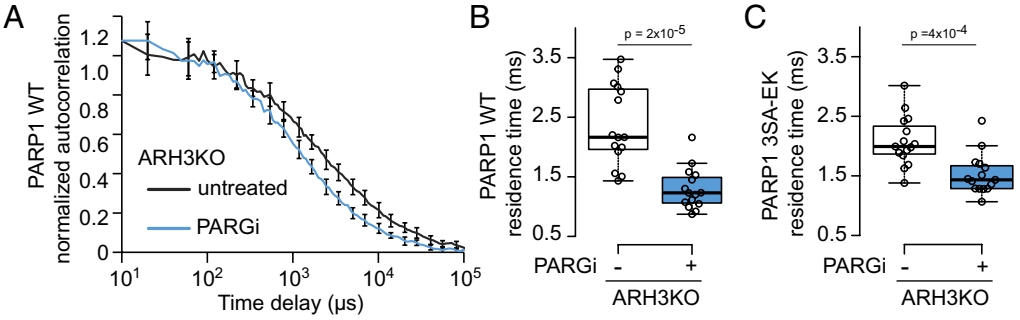

Fig. 3. Spontaneous increase of heteromodification is sufficient to impair PARP1 association with DNA. (*A*) Normalized FCS autocorrelation curves obtained for GFP-tagged PARP1 WT expressed in ARH3 KO cells treated or not with 20 µM of the PARGi PDD00017273 for 48 h. (*B*) Residence times within the focal volume estimated from the fit of the autocorrelation curves shown in (*A*). (*C*) Residence times within the focal volume estimated from the fit of the autocorrelation curves obtained for GFP-tagged PARP1 S499/507/519A E988K (PARP1 3SA-EK) expressed in ARH3 KO cells treated or not with PARGi.

this reduced binding was also observed for the PARP1 3SA-E988K mutant (Fig. 3*C*), heteromodification appears sufficient to repel PARP1 from the DNA.

Histone ADP-Ribosylation Promotes PARP1 Release from DNA Breaks. While hundreds of proteins have been reported to be ADP-ribosylated in the context of the DDR, histones appear as the main target of heteromodification. Moreover, our data above suggest that adding ADPr on chromatin could affect the association of PARP1 with DNA breaks, potentially promoting its mobilization. To test this possibility, we aimed to develop a molecular tool that would be able to specifically erase ADPr moieties bound to histones. We made a fusion between the serine-specific ADP-ribose hydrolase ARH3 and the N-terminal domain of the Latency-Associated Nuclear Antigen (LANA1–32), known to bind to nucleosomes at the folded region of H2A-H2B (40). By immunoblotting, we observed that expressing this LANA-ARH3 construct in ARH3 KO cells cleared histone ADP-ribosylation induced by H_2O_2 genotoxic stress much more efficiently than the expression of ARH3 WT (Fig. 4*A*). Concomitantly, PARP1 automodification appeared similar in ARH3 KO cells expressing ARH3 WT or the LANA-ARH3 fusion. The erasure of histone ADP-ribosylation was not observed with the catalytically dead fusion LANA-ARH3 D77/78N (DD) (41), demonstrating the involvement of the hydrolase activity of ARH3 in this process. Using the previously described LacI-macrodomain fusion to enrich ADP-ribosylated PARP1 at the LacO array, we also observed that expressing LANA-ARH3 did not impact PARP1 automodification consecutive to DNA damage by laser irradiation (Fig. 4 *B* and *C*). Altogether, these results show that prepositioning ARH3 onto chromatin by fusing it to the N-terminal domain of LANA allows for an efficient and specific erasure of histone ADP-ribosylation induced by DNA damage.

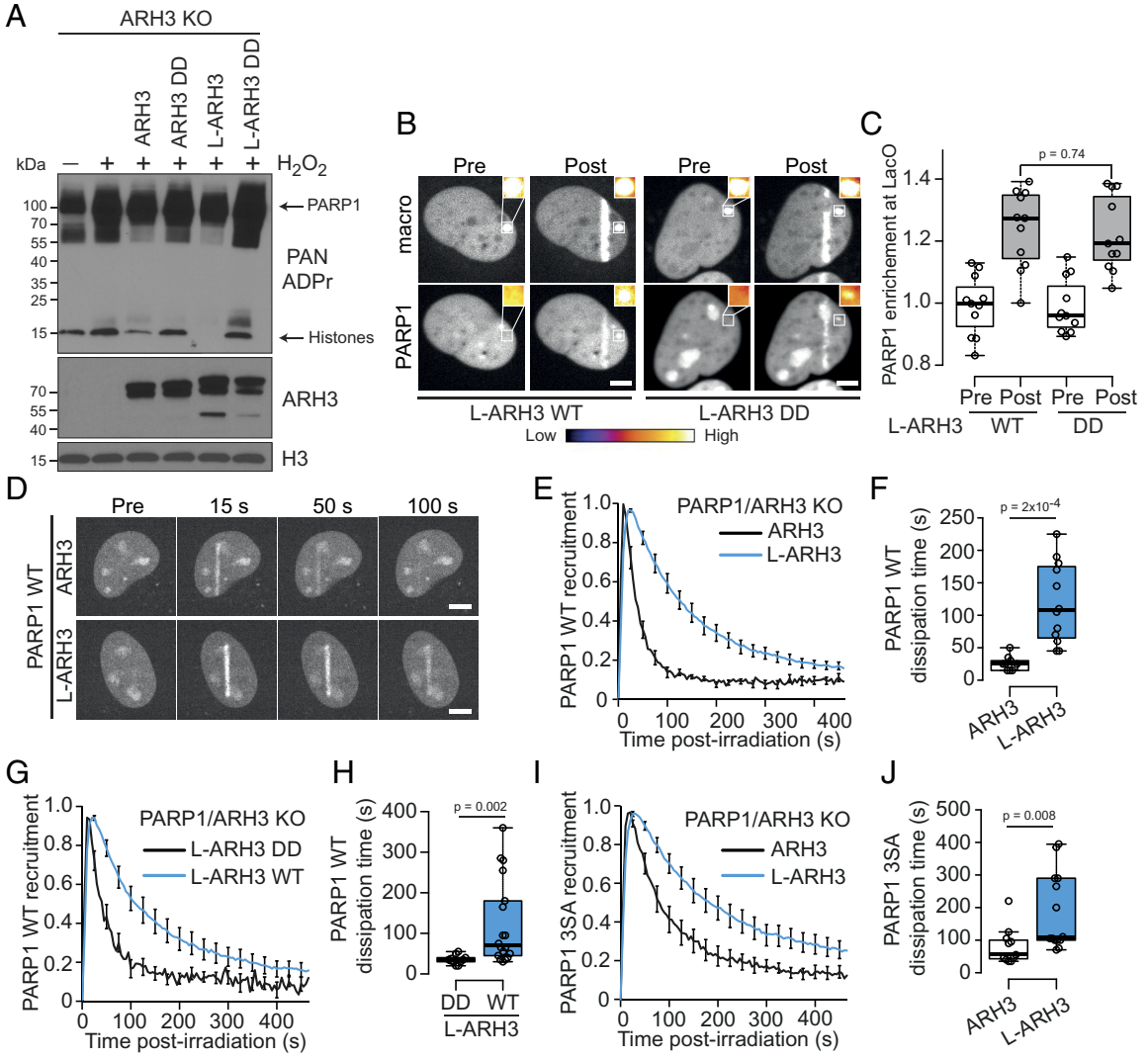

Fig. 4. Histone ADP-ribosylation promotes PARP1 release from DNA breaks. (*A*) Immunoblot of ARH3 KO cells, untransfected, or expressing either GFP-tagged ARH3 WT, ARH3 D77/78N (DD), LANA-ARH3 WT (L-ARH3), or LANA-ARH3 D77/78N (L-ARH3 DD) treated or not with H_2O_2. The blot was stained with a pan-ADPr and an ARH3 antibody. H3 staining was used as loading control. (*B*) Representative images of UO2S cells bearing LacO repeats and coexpressing a mCherry-tagged fusion between the LacI and the macrodomain of macroH2A1.1, PARP1 WT fused to Halotag stained with JF646, and LANA-ARH3 WT or D77/78N tagged with GFP. Images were taken prior to damage and 50 s post 405 nm laser irradiation. *Insets* pseudocolored according to the look-up table displayed below show magnification of the LacO array. (*C*) Quantification of PARP1 accumulation at the LacO array from the images shown in (*B*). (*D–F*) Representative image time courses (*D*), recruitment kinetics (*E*), and dissipation times (*F*) of GFP-tagged PARP1 WT after DNA damage by 405 nm laser irradiation, in PARP1/ARH3 KO coexpressing mCherry-tagged ARH3 WT or LANA-ARH3 WT. (*G* and *H*) Recruitment kinetics (*G*) and dissipation times (*H*) of GFP-tagged PARP1 WT after DNA damage by 405 nm laser irradiation, in PARP1/ARH3 KO coexpressing mCherry-tagged LANA-ARH3 WT or LANA-ARH3 D77/78N. (*I* and *J*) Recruitment kinetics (*I*) and dissipation times (*J*) of GFP-tagged PARP1 3SA after DNA damage by 405 nm laser irradiation, in PARP1/ARH3 KO coexpressing mCherry-tagged ARH3 WT or LANA-ARH3 WT. Scale bar, 5 μm for (*B* and *D*).

Next, we analyzed the recruitment dynamics of GFP-tagged PARP1 WT in PARP1/ARH3 double KO cells (*SI Appendix*, Fig. S3*A*) coexpressing similar levels of mCherry-tagged ARH3 or LANA-ARH3 (*SI Appendix*, Fig. S3*B*) and found that the presence of the latter led to increased PARP1 retention (Fig. 4 *D–F*). Comparing the impact of LANA-ARH3 and the mutant LANA-ARH3 D77/78N showed that this increased trapping of PARP1-WT relied on the hydrolase activity of ARH3 (Fig. 4 *G* and *H* and *SI Appendix*, Fig. S3*C*). The fact that the PARP1 3SA mutant was trapped in the presence of LANA-ARH3 similar to PARP1 WT also demonstrated that this retention was not due to reduced automodification (Fig. 4 *I* and *J* and *SI Appendix*, Fig. S3*D*). In addition, this protrapping effect of the LANA-ARH3 fusion was not observed in cells lacking HPF1, confirming that it relies on the erasure of HPF1-dependent histone ADP-ribosylation (*SI Appendix*, Fig. S3 *E–H*). Importantly, this impact on PARP1 dynamics is not specific to the LANA-ARH3 fusion. Indeed, expressing a fusion between H2B and ARH3, which led to the erasure of histone ADP-ribosylation similar to what was observed with LANA-ARH3, was also associated with slower mobilization of PARP1 at DNA lesions (*SI Appendix*, Fig. S2 *I–Q*). Together, these different results all point toward an important contribution of histone ADP-ribosylation in the timely release of PARP1 from the sites of damage in addition to automodification.

Histone ADP-Ribosylation Underlies Resistance to the PARP Inhibitor Olaparib. It is now firmly established that there is a strong correlation between PARP1 trapping at the DNA lesions and the cytotoxicity of PARPi (17). Therefore, we wondered whether the erasure of histone ADP-ribosylation could sensitize cells to PARPi. U2OS WT or ARH3 KO cells stably expressing mCherry-tagged LANA-ARH3 or ARH3 at similar levels (*SI Appendix*, Fig. S4) were treated with olaparib, a PARP inhibitor currently used in the clinic, and cell survival was assessed by clonogeny (Fig. 5 and *SI Appendix*, Table S1). In line with previous observations, the loss of ARH3 was associated to resistance to PARPi (22) compared to WT cells, which was rescued by the stable expression of mCherry-tagged ARH3. The ARH3 KO cells stably expressing mCherry-tagged LANA-ARH3 were more sensitive to olaparib then WT cells or the ARH3 KO expressing mCherry ARH3. Therefore, the erasure of histone ADP-ribosylation due to LANA-ARH3 was associated with an increase in olaparib toxicity.

Discussion

The discovery of the synthetic lethality between PARPi and BRCA deficiency demonstrated the great potential offered by the targeting of PARP1 for cancer therapies (42, 43). Nevertheless, a major drawback of these PARPi-driven treatments is the high frequency of acquired resistance (20). Therefore, there is a need for a better understanding of the cellular mechanisms modulating PARPi cytotoxicity to foster the improvement of current therapeutic schemes and identify relevant predictive biomarkers. Different factors have been shown to modulate sensitivity to PARPi, in particular those that affect the retention of PARP1 at the DNA lesions (18, 24–28). While it is known for more than a decade that ADP-ribosylation is the central driver of PARP1 timely removal from sites of damage (17, 29), the specific contribution of the different components of this signaling pathway has remained unexplored until recently. Thanks to major advances in the field over the last years, the targets of ADP-ribosylation in the DDR context have now been mapped at the single residue resolution (9, 31, 44), providing a solid basis to identify the targets whose ADP-ribosylation could affect PARP1 trapping. Along this line, HPF1-dependent automodification of S499, S507, and S519 has been shown to promote PARP1 release from DNA breaks (22). Here, we report that heteromodification, and in particular histone ADP-ribosylation also facilitates PARP1 dissipation, thus contributing to cell resistance to PARPi.

Several mechanisms could underlie the ADP-ribosylation-dependent PARP1 mobilization from the lesions. Early in vitro data had shown that electrostatic repulsion between negatively charged ADP-ribosylated PARP1 and DNA promotes the dissociation of the PARP1/DNA complex (45). Nevertheless, it was unclear whether this held true in the chromatin context, where the anionic characteristics of DNA are compensated by the positive charges on histones. By revealing the contribution of histone ADP-ribosylation to PARP1 release, our data support the idea that electrostatic repulsion between automodified PARP1 and chromatin decorated with ADP-ribose moieties could promote PARP1 dissociation from DNA breaks. Furthermore, in light of recent findings suggesting that PARP1 trapping upon PARPi treatment might not be due to impaired dissociation but rather sustained rebinding to the lesions (30), our data imply that histone ADP-ribosylation could act as a shield along the chromatin to

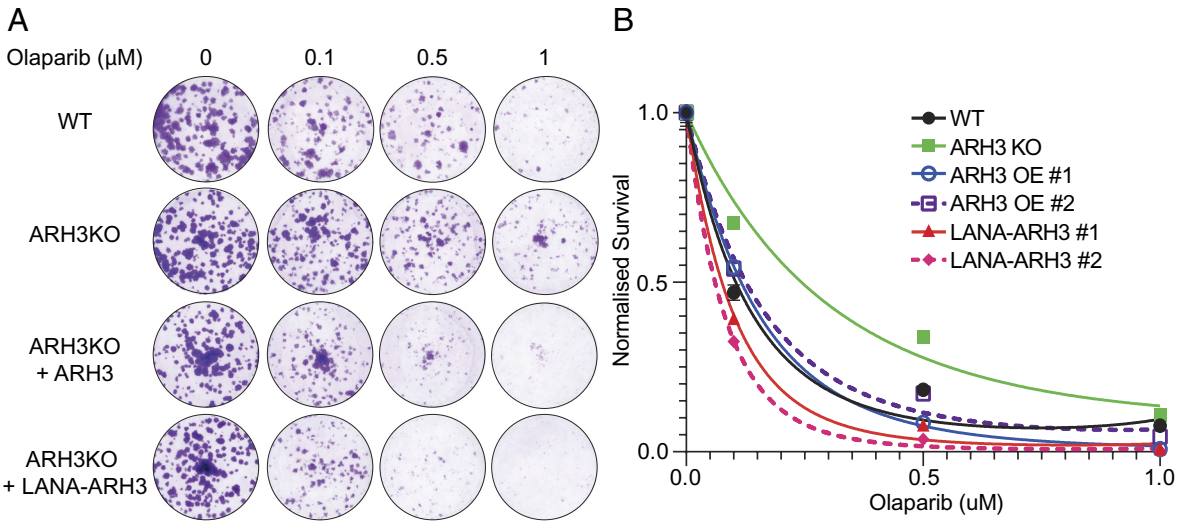

Fig. 5. Histone ADP-ribosylation underlies resistance to the PARP inhibitor olaparib. (*A* and *B*) Representative images of the clonogenic assay (*A*) and cell survival curves (*B*) for WT cells, ARH3 KO cells, two clones of ARH3 KO cells expressing mCherry-tagged ARH3 WT (ARH3 OE), and two clones of ARH3 KO cells expressing mCherry-tagged LANA-ARH3 WT, upon treatment with the PARPi olaparib.

prevent this reassociation. Besides this electrostatic modulation of the dynamic interaction between PARP1 and DNA lesions, histone ADP-ribosylation may also contribute to PARP1 dissipation *via* some more active removal mechanisms. In particular, histone ADP-ribosylation is crucial for the activity of the chromatin remodeler ALC1/CHD1L (46–48), found overexpressed in several tumors (49). Upon binding to ADP-ribosylated nucleosomes in the vicinity of the DNA lesions, ALC1 could peel PARP1 off the damaged chromatin, thus promoting cell resistance to PARPi (18, 25, 26).

Our findings that histone ADP-ribosylation impacts sensitivity to PARPi opens exciting therapeutic perspectives in light of the potential competition of this modification with other histone marks (50). Indeed, a crosstalk between phosphorylation and ADP-ribosylation at serine 10 of histone H3 has been proposed with functional consequences regarding cell cycle progression (51, 52). Furthermore, lysine acetylation or methylation is also thought to impact histone ADP-ribosylation on serines, given that the latter occurs preferentially at lysine-serine motifs upon DNA damage (9, 53, 54). Due to this crosstalk, the fact that histone ADP-ribosylation influences PARP1 trapping opens the possibility to potentiate the cytotoxicity of PARPi by combining them with compounds affecting other histone marks. In fact, this was already reported for histone deacetylase inhibitors, which provided additional cytotoxicity against various tumors when combined with PARPi (55–57). Thus, although further investigation is needed to better understand this synthetic effect, it is tempting to speculate that it could originate from the shut-down of histone ADP-ribosylation consecutive to increased histone acetylation upon treatment with histone deacetylase inhibitor. Finally, taking advantage of the development of new antibodies recognizing ADP-ribosylated histones (12), our results imply that the status of this histone modification could be used as a biomarker to help predict tumor response to PARPi.

Materials and Methods

Plasmids. The plasmids used in this study, pmCherry-PARP1 WT, pmCherry-PARP1 E988K (18) pmCherry-PARP1 3SA (S499A/S507A/S519A) (16) and the GFP-tagged PARP1 chromobody (22), were described previously. pmEGFP-PARP1 3SA (S499A/S507A/S519A) cDNA was generated by amplifying PARP1 3SA cDNA from pDEST-YFP-PARP1-3SA (22) and ligated into pmEGFP-C1 between BglII and XmaI. The macrodomain of macroH2A1.1 was amplified from pcDNA3.1-YFP-macroH2A1.1 macrodomain (34) using primers described *SI Appendix*, Table S1 in *SI Appendix*, Table S2 and ligated into pmCherry-Lac repressor (LacI) (58). pH2B-mCherry-Macrodomain is a ligation of MacroH2A1.1 Macrodomain in pH2B-pmCherry with (BshTI/NdeI). HaloTag was amplified from pBS-SKII-3XHA-HALO-Kanamycin [Addgene #188933, (59)] using primers described *SI Appendix*, Table S1 in *SI Appendix*, Table S2 and ligated into pmEGFP-PARP1 between Bsp1407I and BshTI. PmEGFP-PARP1 3SA-E988K was made using site-directed mutagenesis on PARP1 3SA constructs with primers listed in *SI Appendix*, Table S2. pmCherry-LANA-ARH3, pmCherry-LANA-ARH3 D77-78N, and pmCherry-ARH3 were made using Gibson Assembly (NEB); pmCherry-C1 vector was digested with BamHI and XhoI, and the PCR fragments were amplified from pDEST-YFP-ARH3 (22) and pGFP-LANA 1-32 (40) with primers listed *SI Appendix*, Table S1 in *SI Appendix*, Table S2.

Cell Culture. Routine culture of all cells used in this study was performed in DMEM (Sigma) supplemented with 10% FBS, 100 μg/mL penicillin, and 100 U/mL streptomycin, and maintained at 37 °C in a 5% CO2 incubator. U2OS cells knocked-out for PARP1, PARP1/HPF1, and AHR3 as well as U2OS bearing the LacO array were described previously (3, 11, 60). PARP1/ARH3 and HPF1/ARH3 double knockout cells were obtained by knocking-out PARP1 or HPF1 in ARH3 KO cells as previously described (3). To generate ARH3 KO cells stably expressing mCherry-tagged ARH3 or LANA-ARH3, U2OS ARH3 KO cells were transfected with the appropriate expression plasmids and then selected using media supplemented with 500 μg/mL G418. To induce ADP-ribosylation signaling in ARH3 KO in the absence of genotoxic stress, cells were treated with 20 μM of the PARG inhibitor PDD00017273 (Sigma) for 48 h. For all live-cell experiments, U2OS cells were seeded into 8-well Imaging Chamber CG (Zell-Kontakt) and transfected 48 to 72 h prior to imaging using XtremeGene HP (Roche) according to the manufacturer's instructions. For labeling Halo-tagged PARP1, cells were incubated for 30 min with 10 nM of Janelia Fluor 646 HaloTag Ligand (Janelia Materials) and washed twice with PBS. For cell sensitization prior to laser irradiation at 405 nm, growth medium was aspirated from the Lab-Tek and replaced with fresh medium containing 0.15 to 0.3 μg/mL Hoechst 33342 for 1 h at 37 °C. Immediately prior to imaging, growth medium was replaced with CO_2-independent imaging medium (Phenol Red-free Leibovitz's L-15 medium (Life Technologies) supplemented with 20% fetal bovine serum, 2 mM glutamine, 100 μg/mL penicillin, and 100 U/mL streptomycin). All experiments presented in this work were performed on unsynchronized cells.

Live-Cell Confocal Imaging. PARP1 recruitment dynamics at laser tracks and accumulation at the LacO array were monitored on a spinning disk confocal (Yokogawa CSU-X1 spinning-disk head coupled to an inverted microscope from Nikon) equipped with a Plan APO 60x/1.4 N.A. oil-immersion objective lens and a sCMOS ORCA Flash 4.0 camera. The fluorescence of EGFP and mCherry was excited with lasers at 490 and 561 nm, respectively, and detected with band-pass filters at 500 to 550 nm and 590 to 660 nm, respectively. DNA damage in Hoechst presensitized cells was performed by laser irradiation at 405 nm along a 16 μm-line through the nucleus using galvanometric mirrors coupled to the epifluorescence backboard of the microscope (iLas2 from Roper Scientific). To ensure reproducibility, laser power at 405 nm was measured at the beginning of each experiment and set to 125 μW at the sample level. Recruitment time courses after laser irradiation at 800 nm were completed on a Zeiss LSM 880 confocal setup equipped with a C-Apo ×40/1.2 N.A. water-immersion objective. Nuclei of nonsensitized cells were irradiated within a region of interest of 8 μm width and 1 μm height with a Ti:sapphire femtosecond infrared laser (Mai Tai HP, Spectra-Physics) with emission wavelength set to 800 nm. The pinhole was set to 1 Airy unit, and fluorescence detection was performed on a GaAsP detector array with a pixel size of 80 nm. The fluorescence of GFP and mCherry were excited with lasers at 490 and 561 nm, respectively, and detected within windows ranging from 500 to 550 nm and 580 to 650 nm, respectively. All these live-cell imaging experiments were performed at 37 °C using a heating chamber.

Image Analysis. To assess PARP1 recruitment kinetics, the mean intensities within the damaged region (I_d), the nucleus (I_n), and the background outside of the cell (I_{bg}) were measured by manual segmentation using ImageJ. Protein accumulation at sites of damage (A_d) was then calculated as

$$A_d = \frac{I_d - I_{bg}}{I_n - I_{bg}}.$$

The intensity within the microirradiated area was then subtracted to the intensity prior to damage induction and normalized to the maximum intensity. The characteristic dissipation time used to quantify PARP1 release speed was measured as the time needed to dissipate half of the maximum recruitment intensity on the recruitment curves.

The intensity at the LacO array (A_{lo}) was quantified with the following equation where I_o is the intensity within a region encompassing the LacO array, I_n is the signal in the nucleoplasm devoid of the LacO array and I_{bg} is the intensity of the background:

$$A_{lo} = \frac{I_o - I_{bg}}{I_n - I_{bg}}.$$

The intensity within the LacO array was then normalized to the intensity prior to damage induction.

FRAP. FRAP experiments following DNA damage by laser irradiation were completed on a Zeiss LSM980 confocal setup equipped with a Plan APO 63X/1.4 N.A. oil-immersion objective. The pinhole was set to 1 Airy unit and fluorescence detection was performed on a GaAsP detector array. The fluorescence of GFP was excited at 488 nm and detected within a window ranging from 500 to 550 nm.

The pixel size was set to 87 nm. Nuclei of Hoechst-sensitized cells were irradiated at 405 nm within a region of interest of 11 μm width and 1 μm height to induce DNA damage. Photobleaching of GFP-tagged PARP1 was performed 60 s after damage induction within a circle of 2 μm in diameter using the 488 nm set at full power. These experiments were performed at 37 °C using a heating chamber. To measure the FRAP the mean intensities within the bleached region (I_b), the nucleus (I_n), and the background outside of the cell (I_{bg}) were measured by manual segmentation using ImageJ. Fluorescence recovery (F_r) was then calculated as

$$F_r = \frac{I_b - I_{bg}}{I_n - I_{bg}}.$$

The fluorescence recovery was then normalized to the fluorescence prior to bleaching. These normalized fluorescence recovery were fitted with the following model:

$$F(t) = 1 - A\exp(-t/\tau),$$

where A is the amplitude of the bleach, and τ is the characteristic recovery time.

FCS. FCS experiments were performed on a Zeiss LSM880 confocal setup equipped with a C-Apo 40x/1.2 N.A. water immersion objective. GFP fluorescence was excited with a 488 nm laser and single emitted photons, selected by a bandpass filter at 500 to 550 nm, were detected and counted on a GaAsP spectral detector. The laser power used for FCS measurements was adjusted to minimize photobleaching. Each FCS acquisition lasted 20 s to reduce the noise in the autocorrelation curves. Cells were maintained at 37 °C with a heating chamber. Raw photon traces obtained for GFP-tagged PARP1 were detrended for slow fluctuations and autocorrelated using Fluctuation Analyzer 4G software (61). Autocorrelation curves were fitted with the following effective diffusion model (62):

$$G(t) = \frac{1}{2^{3/2}N}\left(1+\frac{t}{\tau_{res}}\right)^{-1}\left(1+\frac{t}{\omega^2\tau_{res}}\right)^{-1/2},$$

where N is the number of tagged molecules in the focal volume, τ_{res} is the residence time in the focal volume, and ω is the structural parameter of the focal volume, which was fixed to 6.

Western Blotting. U2OS cells were plated in 6 cm dishes and transfected with the indicated plasmids using XtremeGene HP (Roche) according to the manufacturer's instructions 48 h prior to harvest. For the H_2O_2 treatment media were removed from the cells and replaced with fresh cell culture media supplemented with 2 mM H_2O_2 for 7 min. The cells were collected and lysed on Triton-X buffer [1% Triton X-100, 100 mM NaCl, 50 mM Tris-HCl, pH 8.0, 5 mM $MgCl_2$, 0.1% Benzonase (Sigma-Aldrich), and 1× protease inhibitor (Roche)] on an orbital rotator for 30 min at 4 °C. Samples were centrifuged at 15,000 g for 15 min, and the supernatant was collected. Protein samples were quantified using Bradford (Bio-Rad), and equal amounts of protein were loaded on gels for SDS–PAGE prior to immunoblotting. Proteins were transferred onto nitrocellulose membranes (Abersham) and blocked with blocking buffer [5% milk (w/v) in PBS + 0.1% Tween 20] for 30 min. After blocking, membranes were incubated in primary antibody [PAN-ADPr (1:1,500, Sigma, MABE1016), ARH3 (1:1,500, Sigma, hpa027104), H3 (1:5,000, Abcam, Ab1731)] overnight at 4 °C. Membranes were then washed three times with PBS + 0.1% Tween 20, incubated with the Anti-Mouse-HRP (1:3,000, Agilent, P044701-2) or Anti-Rabbit-HRP (1:3,000-8,000, Agilent, P039901-2) for 1 h at room temperature. Membranes were washed three times with PBS + 0.1% Tween20. Membranes were visualized on Hyper ECL films (Cytiva) after incubation with Pierce ECL Western Blotting Substrate (ThermoFisher).

Clonogenic Survival Assay. U2OS WT, ARH3 KO, and ARH3 KO stably expressing mCherry-ARH3 or mCherry-Lana-ARH3 were seeded in triplicate in 12-well plates at a density of 500 cells/well in media containing DMSO or olaparib at a final concentration of 0.1 μM, 0.5 μM, and 1 μM. Colonies were allowed to grow for 11 d before the media were removed, washed once in PBS before cells were fixed, and stained with 0.5% crystal violet in 25% methanol for 30 min. Plates were washed with water and air dried. The area of cell growth was calculated using the ImageJ plugin ColonyArea (63). Colony formation assays were repeated 5 times, and the dose–response curves were analyzed with GraphPad Prism v9.4 software where a linear quadratic survival model was fitted using the formula $Y = 100 * e^{-(AX+BX^2)}$, where Y is the percentage of cells surviving; X the drug dose; A the coefficient for linear killing; and B the coefficient for quadratic killing.

Statistics and Reproducibility. Data analysis and visualization was performed using R software (https://www.r-project.org/). The boxplot limits correspond to the 25th and 75th percentiles and the central line indicates the median value. The whiskers extend 1.5 times the interquartile range. The timelapse curves are the mean ± SEM of 10 to 15 cells per condition. Timelapse curves and boxplots are from a characteristic experiment among at least three independent repeats. P values were calculated using a two-sided Student's t test, assuming unequal variances. The unpaired t test was used for comparing different cell populations, and the paired t test was used when comparing the same cell population pre- and post-DNA damage. Western blots were completed a minimum of three times with a representative experiment presented in figures.

Data, Materials, and Software Availability. All study data are included in the article and/or *SI Appendix*. The raw images are available from the corresponding authors upon request.

ACKNOWLEDGMENTS. We thank the Microscopy-Rennes Imaging Center (BIOSIT, Université de Rennes), member of the national infrastructure France-BioImaging supported by the French National Research Agency (ANR-10-INBS-04), for providing access to the imaging setups, as well as S. Dutertre and X. Pinson for technical assistance on the microscopes. We thank Stephen Buratowski for his gift of the HaloTag containing plasmid and Luke Lavis for sharing the Janelia Fluor 646 HaloTag Ligand. For this work, the S.H.'s group received financial support from the Agence Nationale de la Recherche (ANR-22-CE12-0039 AROSE), the Institut National du Cancer (PLBIO-2019), the Institut Universitaire de France, and the Ligue Contre le Cancer du Grand Ouest (CD53). S.Z., S.H., and R.S. were supported by the Fondation ARC pour la recherche sur le cancer (ARCDOC42022010004560, ARCPJA2022060005190, and PDF20181208405, respectively). The work in Ivan Ahel's laboratory is supported by the Wellcome Trust (210634 and 223107), Biotechnology and Biological Sciences Research Council (BB/R007195/1), Ovarian Cancer Research Alliance (813369), and Cancer Research United Kingdom (C35050/A22284).

1. C. Liu, A. Vyas, M. A. Kassab, A. K. Singh, X. Yu, The role of poly ADP-ribosylation in the first wave of DNA damage response. *Nucleic Acids Res.* **45**, 8129 (2017).
2. M.-F. Langelier, J. L. Planck, S. Roy, J. M. Pascal, Structural basis for DNA damage-dependent poly(ADP-ribosyl)ation by human PARP-1. *Science* **336**, 728–732 (2012).
3. I. Gibbs-Seymour, P. Fontana, J. G. M. Rack, I. Ahel, HPF1/C4orf27 is a PARP-1-interacting protein that regulates PARP-1 ADP-ribosylation activity. *Mol. Cell* **62**, 432–442 (2016).
4. M. J. Suskiewicz *et al.*, HPF1 completes the PARP active site for DNA damage-induced ADP-ribosylation. *Nature* **579**, 598–602 (2020).
5. F.-H. Sun *et al.*, HPF1 remodels the active site of PARP1 to enable the serine ADP-ribosylation of histones. *Nat. Commun.* **12**, 1028 (2021).
6. J. Rudolph, G. Roberts, U. M. Muthurajan, K. Luger, HPF1 and nucleosomes mediate a dramatic switch in activity of PARP1 from polymerase to hydrolase. *Elife* **10**, e65773 (2021).
7. M.-F. Langelier, R. Billur, A. Sverzhinsky, B. E. Black, J. M. Pascal, HPF1 dynamically controls the PARP1/2 balance between initiating and elongating ADP-ribose modifications. *Nat. Commun.* **12**, 6675 (2021).
8. L. Palazzo *et al.*, Serine is the major residue for ADP-ribosylation upon DNA damage. *Elife* **7**, e34334 (2018).
9. I. A. Hendriks *et al.*, The regulatory landscape of the human HPF1- and ARH3-dependent ADP-ribosylome. *Nat. Commun.* **12**, 5893 (2021).
10. E. Barkauskaite, G. Jankevicius, A. G. Ladurner, I. Ahel, G. Timinszky, The recognition and removal of cellular poly(ADP-ribose) signals. *FEBS J.* **280**, 3491–3507 (2013).
11. P. Fontana *et al.*, Serine ADP-ribosylation reversal by the hydrolase ARH3. *Elife* **6**, e28533 (2017).
12. E. J. Longarini *et al.*, Modular antibodies reveal DNA damage-induced mono-ADP-ribosylation as a second wave of PARP1 signaling. *Mol. Cell* **83**, 1743–1760.e11 (2023).
13. A. Ray Chaudhuri, A. Nussenzweig, The multifaceted roles of PARP1 in DNA repair and chromatin remodelling. *Nat. Rev. Mol. Cell Biol.* **18**, 610–621 (2017).
14. M. S. Luijsterburg *et al.*, PARP1 links CHD2-mediated chromatin expansion and H3.3 deposition to DNA repair by non-homologous end-joining. *Mol. Cell* **61**, 547–562 (2016).
15. R. Smith *et al.*, Poly(ADP-ribose)-dependent chromatin unfolding facilitates the association of DNA-binding proteins with DNA at sites of damage. *Nucleic Acids Res.* **47**, 11250–11267 (2019).
16. R. Smith *et al.*, HPF1-dependent histone ADP-ribosylation triggers chromatin relaxation to promote the recruitment of repair factors at sites of DNA damage. *Nat. Struct. Mol. Biol.* **30**, 678–691 (2023), 10.1038/s41594-023-00977-x.
17. J. Murai *et al.*, Trapping of PARP1 and PARP2 by clinical PARP inhibitors. *Cancer Res.* **72**, 5588–5599 (2012).
18. S. Juhász *et al.*, The chromatin remodeler ALC1 underlies resistance to PARP inhibitor treatment. *Sci. Adv.* **6**, eabb8626 (2020).

19. M. P. Dias, S. C. Moser, S. Ganesan, J. Jonkers, Understanding and overcoming resistance to PARP inhibitors in cancer therapy. *Nat. Rev. Clin. Oncol.* **18**, 773–791 (2021).
20. S. M. Noordermeer, H. van Attikum, PARP inhibitor resistance: A tug-of-war in BRCA-mutated cells. *Trends Cell Biol.* **29**, 820–834 (2019).
21. E. Gogola *et al.*, Selective loss of PARG restores PARylation and counteracts PARP inhibitor–mediated synthetic lethality. *Cancer Cell* **35**, 950–952 (2019).
22. E. Prokhorova *et al.*, Serine-linked PARP1 auto-modification controls PARP inhibitor response. *Nat. Commun.* **12**, 4055 (2021).
23. T. A. Hopkins *et al.*, Mechanistic dissection of PARP1 trapping and the impact on in vivo tolerability and efficacy of PARP inhibitors. *Mol. Cancer Res.* **13**, 1465–1477 (2015).
24. M. Gatti, R. Imhof, Q. Huang, M. Baudis, M. Altmeyer, The ubiquitin ligase TRIP12 limits PARP1 trapping and constrains PARP inhibitor efficiency. *Cell Rep.* **32**, 107985 (2020).
25. P. Verma *et al.*, ALC1 links chromatin accessibility to PARP inhibitor response in homologous recombination-deficient cells. *Nat. Cell Biol.* **23**, 160–171 (2021).
26. G. Hewitt *et al.*, Defective ALC1 nucleosome remodeling confers PARPi sensitization and synthetic lethality with HRD. *Mol. Cell* **81**, 767–783.e11 (2021).
27. A. A. Demin *et al.*, XRCC1 prevents toxic PARP1 trapping during DNA base excision repair. *Mol. Cell* **81**, 3018–3030.e5 (2021).
28. D. B. Krastev *et al.*, The ubiquitin-dependent ATPase p97 removes cytotoxic trapped PARP1 from chromatin. *Nat. Cell Biol.* **24**, 62–73 (2022).
29. O. Mortusewicz, J.-C. Amé, V. Schreiber, H. Leonhardt, Feedback-regulated poly(ADP-ribosyl)ation by PARP-1 is required for rapid response to DNA damage in living cells. *Nucleic Acids Res.* **35**, 7665–7675 (2007).
30. Z. Shao *et al.*, Clinical PARP inhibitors do not abrogate PARP1 exchange at DNA damage sites in vivo. *Nucleic Acids Res.* **48**, 9694–9709 (2020).
31. J. J. Bonfiglio *et al.*, Serine ADP-ribosylation depends on HPF1. *Mol. Cell* **65**, 932–940.e6 (2017).
32. V. Rolli, M. O'Farrell, J. Ménissier-de Murcia, G. de Murcia, Random mutagenesis of the poly(ADP-ribose) polymerase catalytic domain reveals amino acids involved in polymer branching. *Biochemistry* **36**, 12147–12154 (1997).
33. S. Eustermann *et al.*, Structural basis of detection and signaling of DNA single-strand breaks by human PARP-1. *Mol. Cell* **60**, 742–754 (2015).
34. G. Timinszky *et al.*, A macrodomain-containing histone rearranges chromatin upon sensing PARP1 activation. *Nat. Struct. Mol. Biol.* **16**, 923–929 (2009).
35. X. Kong, N. M. Wakida, K. Yokomori, Application of laser microirradiation in the investigations of cellular responses to DNA damage. *Front. Phys.* **8**, 597866 (2021).
36. M. S. Satoh, G. G. Poirier, T. Lindahl, Dual function for poly(ADP-ribose) synthesis in response to DNA strand breakage. *Biochemistry* **33**, 7099–7106 (1994).
37. Z. B. Mackey *et al.*, DNA ligase III is recruited to DNA strand breaks by a zinc finger motif homologous to that of poly(ADP-ribose) polymerase. Identification of two functionally distinct DNA binding regions within DNA ligase III. *J. Biol. Chem.* **274**, 21679–21687 (1999).
38. E. Prokhorova *et al.*, Unrestrained poly-ADP-ribosylation provides insights into chromatin regulation and human disease. *Mol. Cell* **81**, 2640–2655.e8 (2021).
39. J. Rudolph, J. Mahadevan, P. Dyer, K. Luger, Poly(ADP-ribose) polymerase 1 searches DNA via a "monkey bar" mechanism. *Elife* **7**, e37818 (2018).
40. A. J. Barbera *et al.*, The nucleosomal surface as a docking station for Kaposi's sarcoma herpesvirus LANA. *Science* **311**, 856–861 (2006).
41. S. Oka, J. Kato, J. Moss, Identification and characterization of a mammalian 39-kDa poly(ADP-ribose) glycohydrolase. *J. Biol. Chem.* **281**, 705–713 (2006).
42. H. E. Bryant *et al.*, Specific killing of BRCA2-deficient tumours with inhibitors of poly(ADP-ribose) polymerase. *Nature* **434**, 913–917 (2005).
43. H. Farmer *et al.*, Targeting the DNA repair defect in BRCA mutant cells as a therapeutic strategy. *Nature* **434**, 917–921 (2005).
44. S. C. Buch-Larsen *et al.*, Mapping physiological ADP-ribosylation using activated ion electron transfer dissociation. *Cell Rep.* **32**, 108176 (2020).
45. A. M. Ferro, B. M. Olivera, Poly(ADP-ribosylation) in vitro. Reaction parameters and enzyme mechanism. *J. Biol. Chem.* **257**, 7808–7813 (1982).
46. L. Bacic *et al.*, Structure and dynamics of the chromatin remodeler ALC1 bound to a PARylated nucleosome. *Elife* **10**, e71420 (2021).
47. J. Mohapatra *et al.*, Serine ADP-ribosylation marks nucleosomes for ALC1-dependent chromatin remodeling. *Elife* **10**, e71502 (2021).
48. K. Tashiro *et al.*, Chemoenzymatic and synthetic approaches to investigate aspartate- and glutamate-ADP-ribosylation. *J. Am. Chem. Soc.* **145**, 14000–14009 (2023).
49. W. Cheng, Y. Su, F. Xu, CHD1L: A novel oncogene. *Mol. Cancer* **12**, 170 (2013).
50. E. Bartlett *et al.*, Interplay of histone marks with serine ADP-ribosylation. *Cell Rep.* **24**, 3488–3502. e5 (2018).
51. J. Brustel *et al.*, Linking DNA repair and cell cycle progression through serine ADP-ribosylation of histones. *Nat. Commun.* **13**, 185 (2022).
52. J. Ferrand *et al.*, Mitotic chromatin marking governs asymmetric segregation of DNA damage. bioRxiv [Preprint] (2023). https://doi.org/10.1101/2023.09.04.556166 (Accessed 5 February 2024).
53. O. Leidecker *et al.*, Serine is a new target residue for endogenous ADP-ribosylation on histones. *Nat. Chem. Biol.* **12**, 998–1000 (2016).
54. G. Liszczak, K. L. Diehl, G. P. Dann, T. W. Muir, Acetylation blocks DNA damage-induced chromatin ADP-ribosylation. *Nat. Chem. Biol.* **14**, 837–840 (2018).
55. R. D. Rasmussen, M. K. Gajjar, K. E. Jensen, P. Hamerlik, Enhanced efficacy of combined HDAC and PARP targeting in glioblastoma. *Mol. Oncol.* **10**, 751–763 (2016).
56. U. Khalid *et al.*, A synergistic interaction between HDAC- and PARP inhibitors in childhood tumors with chromothripsis. *Int. J. Cancer* **151**, 590–606 (2022).
57. L. Ramos *et al.*, A bifunctional PARP-HDAC inhibitor with activity in Ewing Sarcoma. *Clin. Cancer Res.* **29**, 3541–3553 (2023).
58. H. R. Singh *et al.*, A poly-ADP-ribose trigger releases the auto-inhibition of a chromatin remodeling oncogene. *Mol. Cell* **68**, 860–871.e7 (2017).
59. I. Baek *et al.*, A set of Saccharomyces cerevisiae integration vectors for fluorescent dye labeling of proteins. *G3 (Bethesda)* **12**, jkac201 (2022).
60. A. Czarna *et al.*, Structures of Drosophila cryptochrome and mouse cryptochrome1 provide insight into circadian function. *Cell* **153**, 1394–1405 (2013).
61. M. Wachsmuth *et al.*, High-throughput fluorescence correlation spectroscopy enables analysis of proteome dynamics in living cells. *Nat. Biotech.* **33**, 384–389 (2015).
62. A. Michelman-Ribeiro *et al.*, Direct measurement of association and dissociation rates of DNA binding in live cells by fluorescence correlation spectroscopy. *Biophys. J.* **97**, 337–346 (2009).
63. C. Guzmán, M. Bagga, A. Kaur, J. Westermarck, D. Abankwa, ColonyArea: An ImageJ plugin to automatically quantify colony formation in clonogenic assays. *PLoS One* **9**, e92444 (2014).